

PCCP

Accepted Manuscript



This is an *Accepted Manuscript*, which has been through the Royal Society of Chemistry peer review process and has been accepted for publication.

Accepted Manuscripts are published online shortly after acceptance, before technical editing, formatting and proof reading. Using this free service, authors can make their results available to the community, in citable form, before we publish the edited article. We will replace this *Accepted Manuscript* with the edited and formatted *Advance Article* as soon as it is available.

You can find more information about *Accepted Manuscripts* in the [Information for Authors](#).

Please note that technical editing may introduce minor changes to the text and/or graphics, which may alter content. The journal's standard [Terms & Conditions](#) and the [Ethical guidelines](#) still apply. In no event shall the Royal Society of Chemistry be held responsible for any errors or omissions in this *Accepted Manuscript* or any consequences arising from the use of any information it contains.

Atomistic mechanism of *hcp-to-bcc* martensitic transformation in the Ti-Nb system revealed by molecular dynamics simulations

Yang Li , JiaHao Li*, BaiXin Liu

Key Laboratory of Advanced Materials (MOE), School of Materials Science and Engineering, Tsinghua University, Beijing 100084, China

ABSTRACT

Applying the constructed Ti-Nb potentials, molecular dynamics simulations were conducted to investigate the martensitic transformation of $\text{Ti}_{100-x}\text{Nb}_x$ alloys ($x = 5, 10 \dots 25$) from α' phase (*hcp*) to β phase (*bcc*). It is found that the transformation involved four phases, i.e. α' , α'' , *fco* (face-centered orthorhombic), and β phases. The structures of the obtained phases exhibit consistency with experimental data, verifying the validity of atomic simulations. The simulations not only revealed the processes of atomic displacements during the transformation, but also elucidated the underlying mechanism of the martensitic transformation at the atomic level. The martensitic transformation incorporates three types of coinstantaneous deformations i.e. slide, shear as well as extension, and the subsequent lattice constant relaxation. Furthermore, according to the proposed mechanism, the crystallographic correlation between initial α' phase and final β phase has been deduced. The simulation results provide a clear landscape on the martensitic transformation mechanism, facilitating our comprehensive understanding on the phase transition in the Ti-Nb system.

Keywords: martensitic transformation, molecular dynamics simulation, Ti-Nb alloy

* Corresponding author: lijiahao@mail.tsinghua.edu.cn

1. Introduction

Since the discovery of their intriguing properties, shape memory alloys (SMAs) have attracted considerable attention on account of their significant interest for broad applications.¹ Among the SMAs, Ni-Ti alloys are extensively used as practical SMAs due to the remarkable shape memory effect (SME), pseudo-elasticity and corrosion resistance.^{2,3} Lately, the toxic effect of Ni have facilitated researchers to develop Ni-free SMAs e.g. Ti-Nb alloys to be used as biomaterials in orthopedic applications, owing to its good ductility, low Young's moduli and excellent biocompatibility.^{4,5}

The SME of Ti-Nb SMAs originates from the martensitic transformation from body-centered cubic (*bcc*) β phase to orthorhombic α'' martensite.⁴ In fact, the martensitic transformation occurred in the Ti-Nb system involves multiple phases and varies with the concentration of Nb.⁶ Depending on different producing processes, two equilibrium phases (α and β) and four non-equilibrium phases (α' , α'' , ω and τ) can be observed.⁷ All the six phases are identified as metallic solid solutions with different structures. The α and α' phases are hexagonal close packed (*hcp*, $P6_3/mmc$) phases; α'' phase is a base-centered orthorhombic (*Cmcm*) phase; β phase is a *bcc* ($Im\bar{3}m$) phase; ω phase is a hexagonal ($P6/mmm$) phase; τ phase is a body-centered tetragonal (*bct*) phase.^{6,7}

A lot of experimental research have focused on the structural martensitic transformation and the associated morphology and energy changes in the Ti-Nb system.^{4,6,8-12} For instance, Kim et al.⁴ investigate the shape memory effect and superelasticity associated with the martensitic transformation. Bönisch et al.⁶ made an

investigation on the formation of martensites (α' and α'') and their stability by differential scanning calorimetry analysis. It is noted that the martensitic transformation of the Ti-Nb alloys observed in experiment were induced either by temperature variation or by stress. As a matter of fact, the martensitic phase transformation can be induced by chemical compositions as well, which is known as chemically mediated martensitic phase transformation evolved from a supersaturated solid solution.¹³ In addition to the experimental exploration above, Ashish et al.¹⁴ investigated the structure of α'' phase using *ab initio* method. Nevertheless, neither the experimental exploration nor *ab initio* calculation can uncover the realistic process of atomic displacements in martensitic transformation. Furthermore, the detailed atomic mechanism of phase transition hasn't been elucidated either.

Compared with experimental exploration as well as *ab initio* calculations, MD simulation has been frequently used to investigate phase transition^{13,15-18}, especially the martensitic transformation in metallic systems¹⁹⁻²¹. Considering their advantages in modelling the detailed mechanism of phase transformation, MD simulations were conducted in the present research to investigate the martensitic transformation of $\text{Ti}_{100-x}\text{Nb}_x$ alloys ($x = 5, 10 \dots 25$) from α' phase to β phase, using realistic potentials. From the MD simulations, detailed and complete insight into the martensitic transformation was acquired at an atomic level and hereby the transformation mechanism was elucidated, promoting our comprehensive understanding on the phase transition in Ti-Nb system.

2. Constructed Ti-Nb atomic potential

The Ti-Nb potentials were constructed in the light of the long range empirical potential (LREP)²² due to its efficiency and validity in depicting the atomic interactions in transition metallic system, especially for the *bcc* and *hcp* metals. The LREP energy E_i of atom i could be computed by the following equations:

$$E_i = \frac{1}{2} \sum_{j \neq i} V(r_{ij}) - \sqrt{\sum_{j \neq i} \phi(r_{ij})}, \quad (1)$$

$$V(r_{ij}) = (r_{c1} - r_{ij})^m (c_0 + c_1 r_{ij} + c_2 r_{ij}^2 + c_3 r_{ij}^3 + c_4 r_{ij}^4), \quad 0 < r_{ij} \leq r_{c1}, \quad (2)$$

$$\phi(r_{ij}) = \alpha (r_{c2} - r_{ij})^n, \quad 0 < r_{ij} \leq r_{c2}, \quad (3)$$

r_{c1} and r_{c2} are the cutoff distances of LREP. m , n , α , and c_i are the LREP parameters to be determined by the fitting procedure. From Equation (1)-(3), it can be found that the LREP energy and force can converge to zero at the cutoff radii continuously and smoothly, therefore avoiding the energy and force leaps as well as some unphysical behaviors in the simulations.

For the Ti-Nb binary system, Ti-Ti, Nb-Nb and Ti-Nb potentials are required. The potential parameters were determined by fitting them to the lattice constants, cohesive energies, and elastic modulus of Ti, Nb metals, and their intermetallics. To properly describe the distinction of *hcp* and *bcc* structures, large cutoff radii were adopted in the Ti-Nb potentials, as large cutoff radii account for many shells around a specific atom. Considering the absence of experimental data of Ti-Nb intermetallics, *ab initio* calculations based on density functional theory (DFT) were performed using CASTEP.^{23,24} In the *ab initio* calculations, ultrasoft pseudopotentials were employed to represent the electron-ion interaction. The energy cutoff for plane-wave basis was set

700 eV and the Brillouin zone was sampled with the invariable k -points spacing, in which a $20 \times 20 \times 20$ mesh was set for a *bcc* unit cell. The exchange-correlation functional was built according to the generalized gradient approximation of Perdew and Wang²⁵. The convergence tolerance of a unit cell was set 5.0×10^{-6} eV/atom during the calculation. Firstly, geometry optimization was performed to obtain the lattice constants and enthalpies of intermetallics, and next the elastic moduli were computed.

The Ti-Nb LREP parameters determined by fitting are exhibited in Table 1. The lattice constants, cohesive energies, elastic modulus, and bulk modulus of *hcp*-Ti, and *bcc*-Nb reproduced from LREP and obtained in experiment^{26,27} are displayed in Table 2. The properties of Ti-Nb intermetallics reproduced from LREP and obtained from *ab initio* calculations are presented in Tables 3. One can see that the physical properties obtained from LREP and *ab initio* calculations are in good consistency, implying the relevance of the constructed potential.

Another way to further assess the validity of the LREP is to testify whether the LREP is able to express the atomic interactions in a non-equilibrium condition. As a consequence, the equation of state (EOS) from the LREP and the Rose Equation (RE)²⁸ were derived. The EOS for pure metals and intermetallics obtained from LREP and RE are displayed in Figure 1. One sees that the energy curve obtained from the LREP show excellent consistency with RE within the overall variation range of lattice constant, implying the LREP expresses the atomic interactions of the Ti-Nb system at non-equilibrium state well.

3. Molecular dynamics simulation

On account of the Ti-Nb LREP, the $\text{Ti}_{100-x}\text{Nb}_x$ alloys ($x = 5, 10 \dots 25$) alloys were simulated upon the initial supersaturated *hcp* solid solution (α' phase) to observe the martensitic transformation in the Ti-Nb system. The *hcp* solid solutions contain $13 \times 8 \times 8 \times 4 = 3328$ atoms. The x , y , and z axes of the orthorhombic simulation box are parallel to $[11\bar{2}0]$, $[\bar{1}100]$, $[0001]$ crystalline orientations of *hcp* solid solutions, respectively. Periodic boundary conditions were employed in x , y , and z axes. In constructing the Ti-Nb solid solutions, Ti atoms were first created in all the lattice positions, and then replaced stochastically by some Nb atoms to acquire an expected concentration. To exclude the effect of the Nb atom distribution produced by the random substitution, all the MD simulations were repeated five times in the same simulation conditions. The MD simulations were performed in the Parrinello-Rahman constant pressure scheme, and then the time step was 1×10^{-15} s.^{29,30} To achieve a metastable state, the MD simulations ran for 10^5 time steps, i.e. 0.1 nanoseconds at 300 K and at 0 Pa. In order to investigate the martensitic transformation induced by chemical compositions, the stress as well as heating and cooling treatment were not applied in the atomic simulations. To eliminate the impact of pressure on the martensitic transformation, pressure during atomic simulations was set 0 Pa. The pair correlation function $g(r)$ was computed to inspect the variation of atomic configurations of simulated atoms.²² Moreover, the atomic projection and enthalpy variation of simulated atoms were exhibited as well to monitor the phase transition.

4. Results and discussion

From the simulation results, one sees that the repeated MD simulations in the same condition have revealed similar processes of phase transformation, implying the Nb atom distribution generated by random substitution in solid solutions have little impact on the simulations. Inspecting the simulation results of the $\text{Ti}_{100-x}\text{Nb}_x$ ($x = 5, 10 \dots 25$) alloys, it is found that the $\text{Ti}_{95}\text{Nb}_5$ alloy preserved the original *hcp* structure, suggesting that the α' (*hcp*) phase was stable when the atomic concentration of Nb reached 5 %. However, the other Ti-Nb alloys showed similar martensitic transformation from α' (*hcp*) phase to β (*bcc*) phase when the atomic concentration of Nb exceeded 5 %. The above simulation results indicate that the solid solubility of Nb in α' phase is about 5 at.%, which is consistent with the solid solubility exhibited in phase diagram⁷. To further compare the phase stability of Ti-Nb alloys, the formation heats of the Ti-Nb solid solutions were calculated based on the MD simulations. The formation heats of α - $\text{Ti}_{85}\text{Nb}_{15}$, α'' - $\text{Ti}_{85}\text{Nb}_{15}$, and β - $\text{Ti}_{85}\text{Nb}_{15}$ were derived as 0.096 eV/atom, 0.091 eV/atom, and 0.071 eV/atom, respectively. The formation heats of the α and β phases are in the same order of magnitude as those calculated by thermodynamics (several kJ/mol)³¹. The formation heat of α'' - $\text{Ti}_{85}\text{Nb}_{15}$ is also in the same order of magnitude with the *ab initio* calculations¹⁴. The formation heats of the Ti-Nb solid solutions indicate that with the increasing of the concentration of Nb, the stability of α phase decreases, while the stability of β phase increases, revealing similar tendency of the phase stability as the phase diagram⁷. The consistency of the formation heats with

thermodynamics and *ab initio* calculations indicates that the potentials are reliable and valid.

From the simulation results, it can be discovered that the martensitic transformation would take place when the Nb concentration exceeded a critical alloying content. Considering the similarity of the martensitic transformation of the $\text{Ti}_{100-x}\text{Nb}_x$ ($x = 10, 15 \dots 25$) alloys, we take the $\text{Ti}_{85}\text{Nb}_{15}$ alloy as an example to investigate the martensitic transformation from α' phase to β phase.

To inspect the transformation process of $\text{Ti}_{85}\text{Nb}_{15}$ alloy carefully, the atomic projections and pair correlation functions $g(r)$ were checked every 1000 MD time steps. Four crystalline phases of the $\text{Ti}_{85}\text{Nb}_{15}$ alloy have been discovered during the martensite phase transition, which are the initial α' (*hcp*) phase, intermediate α'' (*orthorhombic*) phase, face-centered orthorhombic (*fco*) phase, as well as final β (*bcc*) phase, as shown in Figures 2 and 3. Figures 2 and 3 exhibit the x - y atomic projections and the corresponding pair correlation functions $g(r)$ of simulated alloy at different time steps (1000 steps, 5000 steps, 7000 steps, and 10000 steps), respectively. It can be seen from Figure 2(a) that the simulated alloy has preserved the initial *hcp* lattice, which is verified by the $g(r)$ of typical *hcp* structure in Figure 2(b). From Figure 2(c), one can find that the lattice has shown slight distortion and a new orthorhombic phase formed. One can notice the unit cell of new phase as indicated in Figure 2(c). The formed orthorhombic phase has been identified as α'' phase, of which the lattice constants are $a = 3.1088 \text{ \AA}$, $b = 5.0146 \text{ \AA}$, $c = 4.6761 \text{ \AA}$ and $y = 0.1933$ in Wyckoff position by analyzing the coordinates of the lattice atoms. The lattice structure of α'' phase is in excellent

agreement with the $\text{Ti}_{84}\text{Nb}_{16}$ experimental data³² ($a = 3.1071 \text{ \AA}$, $b = 5.0142 \text{ \AA}$, and $c = 4.6861 \text{ \AA}$ and $y = 0.1928$ in Wyckoff position), which corroborates the formation of the α'' phase. The $g(r)$ of the ideal α'' phase with the same lattice constants as measured is shown by red dots in Figure 2(d), which shows consistency with the $g(r)$ of simulated $\text{Ti}_{85}\text{Nb}_{15}$ alloy and offers further evidence for the formation of α'' phase. It should be noted that only the upper part of the simulated atoms have transformed to α'' phase while the others haven't, as shown in Figure 2(c), which explains the mismatches of $g(r)$ in Figure 2(d).

Figure 3(a) indicate that the α'' phase has turned to a new fcc phase, whose unit cell was marked on the figure. The corresponding lattice constants have been calculated as $a = 3.1885 \text{ \AA}$, $b = 4.7973 \text{ \AA}$, and $c = 4.6957 \text{ \AA}$. The $g(r)$ exhibited in Figure 3(b) reveals that the structure of $\text{Ti}_{85}\text{Nb}_{15}$ alloy is similar to that of ideal fcc crystal, manifesting the formation of newly formed fcc phase. The distinction between the simulated $g(r)$ and the ideal one in Figure 3(b) originates from the fcc lattices with various lattice constants, which is reasonable considering the transient state of fcc lattice during the relaxation toward bcc phase. One can see that the atomic projections in Figure 3(c) are similar to those of the fcc phase in Figure 3(a) and the corresponding $g(r)$ in Figures 3(d) and 3(b) are similar as well. In fact, the phase appeared in Figure 3(c) can be thought as a special fcc structure, of which lattice constants are $a = 3.3068 \text{ \AA}$, $b = 4.6704 \text{ \AA}$, and $c = 4.6630 \text{ \AA}$. The lattice constants of fcc structure can be approximately considered as $\sqrt{2}a = b = c$, which implies that the fcc lattice can be converted to a bcc lattice with the lattice constant of a . From Figure 3(d), it can be

found the $g(r)$ of $\text{Ti}_{85}\text{Nb}_{15}$ alloy and β (*bcc*) phase with the same lattice constant are excellently consistent, confirming the final structure of $\text{Ti}_{85}\text{Nb}_{15}$ alloy as β phase. The MD simulation results manifest that $\text{Ti}_{85}\text{Nb}_{15}$ alloy has gone through the martensitic transformation from initial *hcp* phase to α'' phase, to *fco* phase, and further to final β phase. The four crystalline phases occurred in the transformation have been identified as shown in Figures 2 and 3 by analyzing the lattice structures and comparing the pair correlation functions $g(r)$ of phases with those of idea crystals. These structures of the involved phases are consistent with experimental observations, signifying that the atomic simulation results are valid and credible.

After the identification of the involved phases, the detailed mechanism of the *hcp-to-bcc* martensitic transformation was then elucidated. Figure 4 shows the distributions of atomic density along z axis $\rho(z)$ for the simulated atoms at different times of the martensitic transformation. Figure 4 reveals that the atomic density $\rho(z)$ maintained invariable as the time increased, implying that the layer structure of the lattice remained invariant during the entire phase transition. Considering Figures 2, 3 and 4, one can deduce that the atoms mainly shifts within the layer (x - y plane) during the phase transition. Furthermore, the atomic displacements have been identified as the shear on the $(0\ 1\ \bar{1}\ 0)_{hcp}$ plane along $[\bar{2}\ 1\ 1\ 0]_{hcp}$ (or $[2\ \bar{1}\ \bar{1}\ 0]_{hcp}$) crystallographic orientation.

For the sake of uncovering the atomic displacements during the martensitic transition, the atomic projections (x - y plane) on the second and third layer (z axis) of the simulated alloy are exhibited in Figure 5. To exhibit the atomic displacements of a unit cell in detail, hexagonal atoms is denoted as red dots. Figure 5(a) indicates that the

lattice as well as the marked unit cell has still maintained the initial *hcp* structure. Upon careful inspection on the atomic positions shown in Figure 5(b), one can see the marked atoms on the third layer ($(0\ 0\ 0\ 2)_{hcp}$ plane) have slide $0.053[\bar{1}\ 0\ 1\ 0]_{hcp}$ orientation from $\left[0\ \frac{1}{3}\ -\frac{1}{3}\ \frac{1}{2}\right]_{hcp}$ to $[-0.0527\ 0.333\ -0.2807\ 0.5]_{hcp}$, leading to the formation of α'' phase as shown in the red dot region. The slide was accompanied by slight shear of $(0\ 1\ \bar{1}\ 0)_{hcp}$ plane along the $[\bar{2}\ 1\ 1\ 0]_{hcp}$ during the transition from *hcp* phase to α'' phase. It should be noted that some other atoms on the third layer have slide along the $[1\ \bar{1}\ 0\ 0]_{hcp}$, forming the α'' phase with a different orientation. From Figure 5(c), one sees that the shear of $(0\ 1\ \bar{1}\ 0)_{hcp}$ plane along the $[\bar{2}\ 1\ 1\ 0]_{hcp}$ have increased and the marked atoms on the $(0\ 0\ 0\ 2)_{hcp}$ plane have slid from $[-0.0527\ 0.333\ -0.2807\ 0.5]_{hcp}$ further to the vicinity of $\left[-\frac{1}{6}\ \frac{1}{3}\ -\frac{1}{6}\ \frac{1}{2}\right]_{hcp}$, leading to the destruction of the α'' lattice and formation of the *fco* lattice. The lattice constants of *fco* structure have experienced an extension in the $[1\ 0\ 0]_{fco}$ orientation and a shrink in the $[0\ 1\ 0]_{fco}$ orientation, generating final *bcc* phase, as indicated in Figure 5 (d). Moreover, it is clearly seen from Figure 5 that the transition from α' to *bcc* phase occurred gradually from the upper right atoms of the lattice to the overall atoms and the lattice has sheared along two contrary orientations ($[\bar{2}\ 1\ 1\ 0]_{hcp}$ and $[2\ \bar{1}\ \bar{1}\ 0]_{hcp}$) leading to the formation of two twin boundaries. It can be discovered that the invariant plane (also known as habit plane) is $(0\ 1\ \bar{1}\ 0)_{hcp}$. By comparing the outline of the atomic projections in Figure 5, it is seen that the lattice has experienced little extension along the $[0\ 1\ \bar{1}\ 0]_{hcp}$ (y direction) in addition to the slide and shear.

Other than examining the atomic projections, the enthalpy variation is presented in Figure 6 to observe the correlation between the enthalpy and the phase. The blue circles and curve in Figure 6 manifests that the *hcp* solid solutions started to transform to α'' phase after a relaxation period of 0.005 ns. Once the phase transformation began, the enthalpy initiated to decrease rapidly with time. When the time reached 0.007 ns, the simulated $\text{Ti}_{85}\text{Nb}_{15}$ alloy had transformed from the α'' phase to *fco* phase. In the subsequent period, the *fco* lattice constants relaxed in the $[1\ 0\ 0]_{fco}$, $[0\ 1\ 0]_{fco}$, and $[0\ 0\ 1]_{fco}$ crystalline orientations, therefore forming the *bcc* (β) lattice. It is found that the *hcp-to-bcc* martensitic transformation costs approximately 0.01 ns. Therefore, one can assess the velocity of martensitic transition as about 400 m/s, indicating consistency with the velocities of representative martensitic transformations³³. Besides, the enthalpy variations of the simulated atoms initiated from *fco* and *bcc* structures are presented in Figure 6 for contrast as well. One notice that the simulated atoms initiated from *fco* structure relaxed swiftly to the *bcc* structure, while the simulated atoms initiated from *bcc* structure remained invariable, manifesting that *bcc* phase is the metastable phase for the $\text{Ti}_{85}\text{Nb}_{15}$ alloy. All the three simulated lattice have turned into the *bcc* structure with the same lattice constant, but the enthalpy hasn't converged to the same. This is caused by the interface energy of the twin boundaries in the simulated lattice initiated from *hcp* lattice. According to the enthalpy difference (0.007 eV/atom) showed in Figure 6, the interface energy of the two twin boundaries is estimated to be $0.128\ \text{J/m}^2$ on average, which is consistent with the same order of magnitude of the experimental twin interface energy³⁴.

One may notice that the $\text{Ti}_{85}\text{Nb}_{15}$ alloy transformed to β phase in the simulation at 300K, implying a distinction from the $\alpha + \beta$ phases in the phase diagram⁷. The phase diagram involves the equilibrium phases which requires a large amount of relaxation time to diffuse and form the interface of phase boundary. Nevertheless, the MD simulations have focused on the diffusionless martensitic transformation involving metastable phases, which is clearly different from the equilibrium phase diagram. As a result, the $\text{Ti}_{85}\text{Nb}_{15}$ alloy has transformed to single β phase, not the $\alpha + \beta$ phases in the phase diagram⁷.

To elucidate the detailed mechanism of Ti-Nb martensitic transformation, the whole *hcp-to-bcc* phase transition can be partitioned into three processes based on the involved phases, i.e. *hcp to α''* transition, *α'' to fco* transition, and *fco to bcc* transition. According to the above discussion on the atomic projections, slide and little shear occurred in the *hcp to α''* transition; while slide, shear and extension proceeded in the *α'' to fco* transition and subsequently *fco* lattice constant extended in the $[1\ 0\ 0]_{fco}$ orientation and shrank in the $[0\ 1\ 0]_{fco}$ orientation in the *fco to bcc* transition. To vividly view the transition processes and geometric correlation between the involved phases, Figures 7 and 8 were plotted as exhibited as follows. Figure 7 illustrates the schematic of geometric relationships among initial *hcp*, α'' and *fco* lattices as well as the corresponding atomic displacements. From Figure 7, one can see that atoms on $(0\ 0\ 0\ 2)_{hcp}$ plane firstly slid $0.053[\bar{1}\ 0\ 1\ 0]_{hcp}$ (indicated by cyan arrow) from $\begin{bmatrix} 0 & \frac{1}{3} & -\frac{1}{3} & \frac{1}{2} \end{bmatrix}_{hcp}$ to $[-0.0527\ 0.333\ -0.2807\ 0.5]_{hcp}$; secondly, the lattice went through a uniform shear γ on $(0\ 1\ \bar{1}\ 0)_{hcp}$ plane along the $[\bar{2}\ 1\ 1\ 0]_{hcp}$ orientation (expressed by

blue arrow), forming the α'' phase (marked by blue dots and lines); thirdly, atoms on $(0\ 0\ 2)_{hcp}$ plane continued sliding $0.114[\bar{1}\ 0\ 1\ 0]_{hcp}$ further to the face center of the lattice (shown by purple arrow); finally, the lattice experienced an extension λ along $[0\ 1\ \bar{1}\ 0]_{hcp}$ direction (signified by orange arrow), forming the *fco* structure. In fact, the two-stage slide, uniform shear and extension have proceeded at the same time. The sequence in Figure 7 was set for the convenience of elucidating the phase transformation mechanism. Figure 8 signifies the geometrical relationship between the *fco* and *bcc* structures. It should be noticed that the *fco* lattice constants went through an adjustment in the *fco-to-bcc* transition, which was not shown in Figure 8. One can clearly see that the *y* and *z* axes of *bcc* lattice can be seen as a clockwise 45° rotation of those of relaxed *fco* lattice, while the *x* axis keeps invariable.

Further, the quantitative geometrical relationships among the phases involved in the transformation were deduced. Suppose that *a* and *c* represent the lattice constants of initial *hcp* structure, and *a'*, *b'* and *c'* with $\kappa = b'/a'$ express those of the *fco* structure. As illustrated in Figure 7, lattice points *A* and *B* have remained the original positions, while points *C*, *D* and *E* have transformed to *C''*, *D''* and *E''*. According to the geometric constraint that *AD''* and *BC''* are perpendicular, the relations between the deforming parameters γ and λ can be deduced. After appropriate mathematic derivations, the relationship between deforming parameters γ and λ can be expressed as

$$\left\{ \begin{array}{l} \kappa = \frac{\sqrt{(\tan \gamma - \sqrt{3})^2 + (1 + \lambda)^2}}{\sqrt{(\tan \gamma + \frac{\sqrt{3}}{3})^2 + (1 + \lambda)^2}} \\ (\tan \gamma - \sqrt{3}) \cdot (\tan \gamma + \frac{\sqrt{3}}{3}) + (1 + \lambda)^2 = 0 \end{array} \right. \quad (4)$$

The correlation between the lattice constants of *hcp* and *fco* lattices is denoted as

$$AB = a = \frac{1}{2} \cdot \sqrt{a'^2 + b'^2} \quad (5)$$

The Equations (4) and (5) express the crystallographic constraints during the transition from *hcp* to *fco* lattice. In general, it's difficult to directly measure the deforming parameters γ and λ . However, they can be derived through Equation (4), as long as the *fco* lattice constants are measured. In addition to the measurement of lattice constants, the angles φ and ϕ (as shown in Figure 7) can be directly measured from the *fco* phase as well. Based on the geometrical correlation indicated in Figure 7, the relations between the angles (φ and ϕ) and the deforming parameters (γ and λ) can be expressed as

$$\varphi = \arctan \frac{\tan \gamma}{1 + \lambda} \quad (6)$$

$$\phi = \arctan \frac{\sqrt{3}(1 + \lambda)}{1 + \sqrt{3} \tan \gamma} \quad (7)$$

To confirm the validity of Equations (4)-(7), we input the *fco* lattice constants, $a' = 3.1885 \text{ \AA}$, $b' = 4.7973 \text{ \AA}$, and $c' = 4.6957 \text{ \AA}$ into the Equations (4)-(7), and obtained $a = 2.8801 \text{ \AA}$, $\gamma = 7.4^\circ$, $\lambda = 0.0646$, $\varphi = 7.0^\circ$, and $\phi = 56.4^\circ$. The lattice constant of initial *hcp* structure $a = 2.92 \text{ \AA}$, and the measured values from *fco* phase are $\varphi = 7.4^\circ$ and $\phi = 55.8^\circ$, which are in accordance with the calculated values. The self-consistency between the measured parameters and the calculated parameters has corroborated that the proposed transformation mechanism from *hcp* phase to *fco* phase is valid and credible.

Moreover, in the light of the coordinate systems shown in Figure 7, the geometric relationship between *hcp* and *fco* lattices is able to be derived solely. Suppose that any crystal orientation $[u \ v \ t \ w]$ ($t = -(u + v)$) and any crystal face $(h \ k \ i \ l)$ ($i = -(h + k)$)

of the *hcp* structure transform to the crystal orientation $[u' v' w']$ and crystal face $(h' k' l')$ of the *fco* structure. The relation matrix of the crystal orientation and crystal face between *hcp* and *fco* lattices is calculated as

$$\begin{pmatrix} u' \\ v' \\ w' \end{pmatrix} = \begin{pmatrix} 0 & -\frac{3}{2} & 0 \\ 1 & \frac{1}{2} & 0 \\ 0 & 0 & 1 \end{pmatrix} \begin{pmatrix} f(u) \\ v \\ w \end{pmatrix} \quad (8)$$

$$\begin{pmatrix} h' \\ k' \\ l' \end{pmatrix} = \begin{pmatrix} 0 & -1 & 0 \\ 2 & 1 & 0 \\ 0 & 0 & 1 \end{pmatrix} \begin{pmatrix} h \\ k \\ l \end{pmatrix} \quad (9)$$

where $f(x)$ is one function defined to generate the slide of $(0\ 0\ 0\ 2)_{hcp}$ plane, which is expressed as

$$f(x) = \begin{cases} x & \text{if an atom locates in the } (0\ 0\ 0\ 1) \text{ plane,} \\ x - \frac{1}{6} & \text{if an atom locates in the } (0\ 0\ 0\ 2) \text{ plane,} \end{cases} \quad (10)$$

The Equations (8) and (9) reveals the crystallographic correlation between *hcp* lattice and *fco* lattice, i.e., $[2\ \bar{1}\ \bar{1}\ 0]_{hcp} \parallel [1\ 1\ 0]_{fco}$, $[0\ 0\ 0\ 1]_{hcp} \parallel [0\ 0\ 1]_{fco}$, $(0\ 1\ \bar{1}\ 0)_{hcp} \parallel (\bar{1}\ 1\ 0)_{fco}$, $(0\ 0\ 0\ 1)_{hcp} \parallel (0\ 0\ 1)_{fco}$.

The *fco* structure has turned into the *bcc* structure when the *fco* lattice relaxed and adjusted its lattice constants (a increased while b decreased and c showed little variation) to $\sqrt{2}a = b = c$. Figure 8 illustrates the geometrical relationship between the *fco* and *bcc* structures. Suppose that any crystal orientation $[u' v' w']$ and any crystal face $(h' k' l')$ in the *fco* structure transform to the crystal orientation $[u'' v'' w'']$ and crystal face $(h'' k'' l'')$ in the *bcc* structure. The relation matrix of the crystal orientation and crystal face between *fco* and *bcc* structures is also denoted as

$$\begin{pmatrix} u'' \\ v'' \\ w'' \end{pmatrix} = \begin{pmatrix} 1 & 0 & 0 \\ 0 & 1 & 1 \\ 0 & -1 & 1 \end{pmatrix} \begin{pmatrix} u' \\ v' \\ w' \end{pmatrix} \quad (11)$$

$$\begin{pmatrix} h'' \\ k'' \\ l'' \end{pmatrix} = \begin{pmatrix} 1 & 0 & 0 \\ 0 & \frac{1}{2} & \frac{1}{2} \\ 0 & -\frac{1}{2} & \frac{1}{2} \end{pmatrix} \begin{pmatrix} h' \\ k' \\ l' \end{pmatrix} \quad (12)$$

The Equations (11) and (12) reveals the crystallographic correlation between *fco* lattice and *bcc* lattice, i.e., $[1\ 0\ 0]_{fco} \parallel [1\ 0\ 0]_{bcc}$, $[0\ 1\ 0]_{fco} \parallel [0\ 1\ \bar{1}]_{bcc}$, $(1\ 0\ 0)_{fco} \parallel (1\ 0\ 0)_{bcc}$, $(0\ 1\ 0)_{fco} \parallel (0\ 1\ \bar{1})_{bcc}$.

Combining Equations (8) - (12), the correlation matrix between the crystal orientation and crystal face for *hcp* and *bcc* structures, denoted as

$$\begin{pmatrix} u'' \\ v'' \\ w'' \end{pmatrix} = \begin{pmatrix} 0 & -\frac{3}{2} & 0 \\ 1 & \frac{1}{2} & 1 \\ -1 & -\frac{1}{2} & 1 \end{pmatrix} \begin{pmatrix} f(u) \\ v \\ w \end{pmatrix} \quad (13)$$

$$\begin{pmatrix} h'' \\ k'' \\ l'' \end{pmatrix} = \begin{pmatrix} 0 & -1 & 0 \\ 1 & \frac{1}{2} & \frac{1}{2} \\ -1 & -\frac{1}{2} & \frac{1}{2} \end{pmatrix} \begin{pmatrix} h \\ k \\ l \end{pmatrix} \quad (14)$$

The Equation (12) reveals the crystallographic correlation between *hcp* lattice and *bcc* lattice, i.e., $[2\ \bar{1}\ \bar{1}\ 0]_{hcp} \parallel [1\ 1\ \bar{1}]_{bcc}$, $[0\ 0\ 0\ 1]_{hcp} \parallel [0\ 1\ 1]_{bcc}$, $(0\ 1\ \bar{1}\ 0)_{hcp} \parallel (\bar{2}\ 1\ 1)_{bcc}$, $(0\ 0\ 0\ 1)_{hcp} \parallel (0\ 1\ 1)_{bcc}$.

To sum up, the detailed crystallographic correlation between the phases involved in the *hcp-to-bcc* martensitic transformation can be acquired through the Equations (4)-

(14). The deduced crystallographic correlations were compared with related observations in experiment to testify the validity of the proposed atomic mechanism. The experimental investigation on the martensitic transformation of Ti-Nb alloys has revealed the crystallographic correlation between α'' and bcc phases as $[1\ 0\ 0]_{\alpha''} \parallel [1\ 0\ 0]_{bcc}$, $[0\ 1\ 0]_{\alpha''} \parallel [0\ 1\ 1]_{bcc}$, $[0\ 0\ 1]_{\alpha''} \parallel [0\ 1\ \bar{1}]_{bcc}$.⁴ The fco lattice can be considered as a sliding of atoms on the $(0\ 0\ 2)_{\alpha''}$ and slight lattice adjustment based on the orthorhombic α'' phase, result in similar crystal orientation between fco and α'' lattices. The crystallographic correlation between α'' and bcc phases can be inferred from that between fco and bcc phases shown in Equations (11) and (12), which exhibits excellent consistency with the experimental investigation. The experimental research on the martensitic transformation from α -Ti to β -Ti has indicated the crystallographic correlation between hcp and bcc phases as $(1\ \bar{1}\ 0\ 0)_{hcp} \parallel (\bar{1}\ 1\ 2)_{bcc}$, $(0\ 0\ 0\ 1)_{hcp} \parallel (0\ 1\ 1)_{bcc}$ ³⁵, which matches well with the Equations (13) and (14) on the condition that the x axis and z axis of bcc lattice are exchanged. The crystallographic correlation between the hcp , α'' and bcc phases have been verified by experimental observations, manifesting the proposed transformation path and mechanism are authentic and valid.

It is also found that during the relaxation process from fco phase toward bcc phase, a body-centered tetragonal (bct) phase formed when the fco structure adjusted its lattice constants to $b = c \neq \sqrt{2}a$. Both the bct and bcc structure can be regarded as special fco structure, the crystallographic correlation also satisfy the Equations (4)-(14).

Next, we focus on the impact and significance of the atomistic martensitic transformation mechanism from α' phase to β phase. The martensitic transformation in

the present study involved α' , α'' , fcc , bcc , and β phases, including most of the metastable phases observed in experiment. The transformation mechanism manifests that the slide, shear, and extension are three basic deformation modes for the martensitic transformation and thereby twin boundaries are often formed due to shearing, which is testified by experimental observations in the Ti-Nb system⁸. The transformation mechanism revealed in the present study also provides a clear landscape on the atomic-level transformation path between the five phases, especially on the transformation path from α'' phase to β phase. The transformation from β phase to α'' phase can be considered as the reverse transformation process from α'' phase to β phase. As a consequence, the transformation path from β phase to α'' phase may be deduced as a transformation from β phase to fcc phase and further to α'' phase. The transformation mechanism from β phase to α'' phase and crystallographic correlation can refer to those of the transformation from α'' phase to β phase, which contributes to our understanding on the shape memory effect of Ti-Nb alloys.

5. Concluding remarks

Applying the realistic Ti-Nb potentials, MD simulations were conducted to investigate the martensitic transformation of $Ti_{100-x}Nb_x$ alloys ($x = 5, 10 \dots 25$) from α' phase to β phase at the atomic level. The simulation results reveal the transformation path between the involved phases (α' , α'' , fcc , and β) and the corresponding crystallographic correlation of the four lattices. The underlying martensite transition mechanism has been elucidated, which has been certified to be realistic and credible by

the self-consistency between the measured parameters and the calculated parameters. The martensitic transformation comprises three coinstantaneous deformations i.e. slide, shear as well as extension, and the latter lattice constant relaxation. The crystallographic correlations between the involved phases have been deduced as well. The proposed mechanism of the martensitic transformation offers a reference for the transformation from β phase to α'' phase, facilitating our comprehensive understanding on the martensitic transformation and SME of the Ti-Nb alloys.

Acknowledgements

The authors appreciate the financial support from the National Natural Science Foundation of China (51131003), the Ministry of Science and Technology of China (973 Program 2011CB606301, 2012CB825700) and the Administration of Tsinghua University.

References:

- 1 A. Biesiekierski, J. Wang, M. A. Gepreel, and C. Wen, *Acta Biomater.*, 2012, **8**, 1661-1669.
- 2 W. Cai, X. L. Meng and L. C. Zhao, *Curr. Opin. Solid St. M.*, 2005, **9**, 296-302.
- 3 K. Otsuka and X. Ren, *Prog. Mater. Sci.*, 2005, **50**, 511-678.
- 4 H. Y. Kim, Y. Ikehara, J. I. Kim, H. Hosoda, and S. Miyazaki, *Acta Mater.*, 2006, **54**, 2419-2429.
- 5 M. Geetha, A. K. Singh, R. Asokamani, and A. K. Gogia, *Prog. Mater. Sci.*, 2009, **54**, 397-425.
- 6 B. Matthias, C. Mariana, W. Thomas, P. Ajit, Z. Michael, G. Annett, S. Werner, and E. Juergen, *Sci. Technol. Adv. Mater.*, 2013, **14**
- 7 Asm, *Alloy Phase Diagrams - ASM Handbook vol 3*. 1992, ASM International, Materials Park.
- 8 Y. W. Chai, H. Y. Kim, H. Hosoda, and S. Miyazaki, *Acta Mater.*, 2009, **57**, 4054-4064.
- 9 D. H. Ping, C. Y. Cui, F. X. Yin, and Y. Yamabe-Mitarai, *Scripta Mater.*, 2006, **54**, 1305-1310.
- 10 Y. B. Wang and Y. F. Zheng, *Mater. Lett.*, 2008, **62**, 269-272.
- 11 J. Ma, I. Karaman, H. J. Maier, and Y. I. Chumlyakov, *Acta Mater.*, 2010, **58**, 2216-2224.
- 12 M. Tahara, H. Y. Kim, H. Hosoda, and S. Miyazaki, *Acta Mater.*, 2009, **57**, 2461-2469.

- 13 J. H. Li and B. X. Liu, *J. Phys. Soc. Jpn*, 2005, **74**, 2699-2702.
- 14 A. Pathak, S. Banumathy, R. Sankarasubramanian, and A. K. Singh, *Comp. Mater. Sci.*, 2014, **83**, 222-228.
- 15 K. Takakura, T. Ueda, K. Miyakubo, and T. Eguchi, *Phys. Chem. Chem. Phys.*, 2013, **15**, 279-290.
- 16 K. Lai, B. Wang, Y. Zhang, and Y. Zhang, *Phys. Chem. Chem. Phys.*, 2012, **14**, 5744-5752.
- 17 K. Mochizuki, K. Himoto and M. Matsumoto, *Phys. Chem. Chem. Phys.*, 2014, **16**, 16419-16425.
- 18 J. H. Li, H. B. Guo and B. X. Liu, *Acta Mater.*, 2005, **53**, 743-748.
- 19 K. Saitoh, T. Sato and N. Shinke, *Mater. Trans.*, 2006, **47**, 742-749.
- 20 G. J. Ackland, A. P. Jones and R. Noble-Eddy, *Mat. Sci. Eng. A.-Struct.*, 2008, **481**, 11-17.
- 21 G. P. P. Pun and Y. Mishin, *J. Phys.-Condens. Mat.*, 2010, **22**
- 22 J. H. Li, Y. Dai, X. D. Dai, T. L. Wang, and B. X. Liu, *Comp. Mater. Sci.*, 2008, **43**, 1207-1215.
- 23 M. D. Segall, P. J. Lindan, M. J. Probert, C. J. Pickard, P. J. Hasnip, S. J. Clark, and M. C. Payne, *J. Phys.-Condens. Mat.*, 2002, **14**, 2717.
- 24 S. J. Clark, M. D. Segall, C. J. Pickard, P. J. Hasnip, M. I. Probert, K. Refson, and M. C. Payne, *Z. Kristallog.*, 2005, **220**, 567-570.
- 25 J. P. Perdew and Y. Wang, *Phys. Rev. B*, 1992, **45**, 13244.
- 26 C. Kittel, *Introduction to solid state physics*. 1996, Wiley New York.

- 27 G. Simmons and H. Wang, *Single crystal elastic constants and calculated aggregate properties: A handbook 2nd ed.* 1971, MIT Press, Cambridge.
- 28 J. H. Rose, J. R. Smith, F. Guinea, and J. Ferrante, *Phys. Rev. B*, 1984, **29**, 2963.
- 29 M. Parrinello and A. Rahman, *J. Appl. Phys.*, 1981, **52**, 7182.
- 30 M. P. Allen and D. J. Tildesley, *Computer simulation of liquids.* 1987, Oxford University Press, London.
- 31 F. R. De Boer, R. Boom, W. C. M. Mattens, A. R. Miedema, and A. K. Niessen, *Cohesion in metals: transition metal alloys.* 1988, North-Holland, Amsterdam.
- 32 S. Banumathy, R. K. Mandal and A. K. Singh, *J. Appl. Phys.*, 2009, **106**
- 33 D. A. Porter and K. E. Easterling, *Phase Transformation in Metals and Alloys.* 1992, CRC press, Boca Raton.
- 34 R. W. Cahn and P. Haasen, *Physical Metallurgy 4th ed.* 1996, North Holland, Amsterdam.
- 35 W. Zhang, W. S. Zhao, D. X. Li, and M. L. Sui, *Appl. Phys. Lett.*, 2004, **84**, 4872-4874.

Tables

Table 1. The LREP parameters for the Ti-Nb system.

	Ti	Nb	Ti-Nb
m	4	4	4
n	4	8	6
r_{c1} (Å)	5.795909	4.802790	5.269705
r_{c2} (Å)	6.957239	6.818734	6.933926
c_0 (10^{-19} J)	0.549500	16.724606	0.644717
c_1 (10^{-19} J/Å ^{m+1})	-0.623598	-22.895200	-0.973843
c_2 (10^{-19} J/Å ^{m+2})	0.273602	11.810592	0.612069
c_3 (10^{-19} J/Å ^{m+3})	-0.054871	-2.696127	-0.173700
c_4 (10^{-19} J/Å ^{m+4})	0.004280	0.228753	0.018338
α (10^{-19} J/Å ⁿ)	0.032226	0.000473	0.004248

Table 2. Physical properties (Lattice constants (a , c Å), Cohesive energies (E_c , eV), Bulk modulus (B_0 , Mbar), Elastic constants (C_{ij} , Mbar)) of *hcp*-Ti and *bcc*-Nb obtained from the LREP and experimental data.

	<i>hcp</i> -Ti		<i>bcc</i> -Nb	
	fitted	expt	fitted	expt
a (Å)	2.946	2.95	3.300	3.300
c (Å)	4.681	4.68		
E_c (eV)	4.845	4.85	7.570	7.570
C_{11} (Mbar)	1.647	1.624	2.655	2.465
C_{12} (Mbar)	0.729	0.92	1.249	1.345
C_{13} (Mbar)	0.683	0.69		
C_{33} (Mbar)	1.863	1.807		
C_{44} (Mbar)	0.412	0.467	0.199	0.287
B_0 (Mbar)	1.039	1.05	1.718	1.718

Table 3. Physical properties of the Ti-Nb intermetallics reproduced from the LREP (first line) and obtained from *ab initio* calculations (second line).

	Ti ₃ Nb	TiNb	TiNb ₃
	L1 ₂	B ₂	L1 ₂
a (Å)	4.139	3.288	4.188
	4.123	3.263	4.183
E_c (eV)	5.467	6.116	6.670
	5.446	6.135	6.666
B_0 (Mbar)	1.338	1.376	1.159
	1.236	1.365	1.346

Figure captions

Figure 1. The potential energy variation with lattice constant obtained from the LREP (green solid line) and RE (red dotted line) for (a) Ti, (b) Nb, and (c) B₂ TiNb intermetallics, respectively.

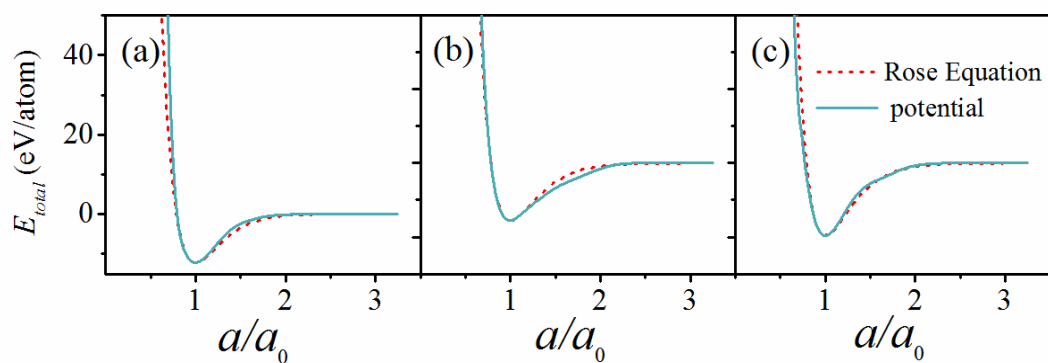


Figure 2. The atomic projections (x - y plane) and corresponding pair correlation functions $g(r)$ of $\text{Ti}_{85}\text{Nb}_{15}$ alloy at (a), (b) 1000 time steps and (c), (d) 5000 time steps, respectively.

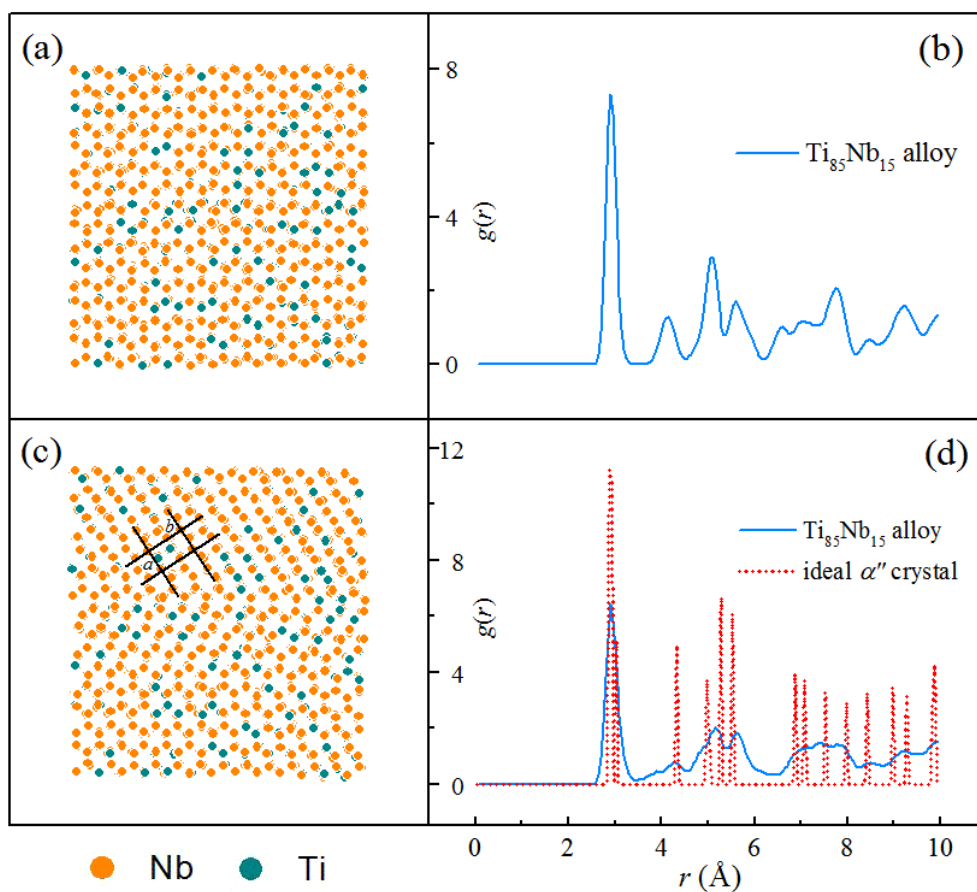


Figure 3. The atomic projections (x - y plane) and corresponding pair correlation functions $g(r)$ of $\text{Ti}_{85}\text{Nb}_{15}$ alloy at (a), (b) 7000 time steps and (c), (d) 10000 time steps, respectively.

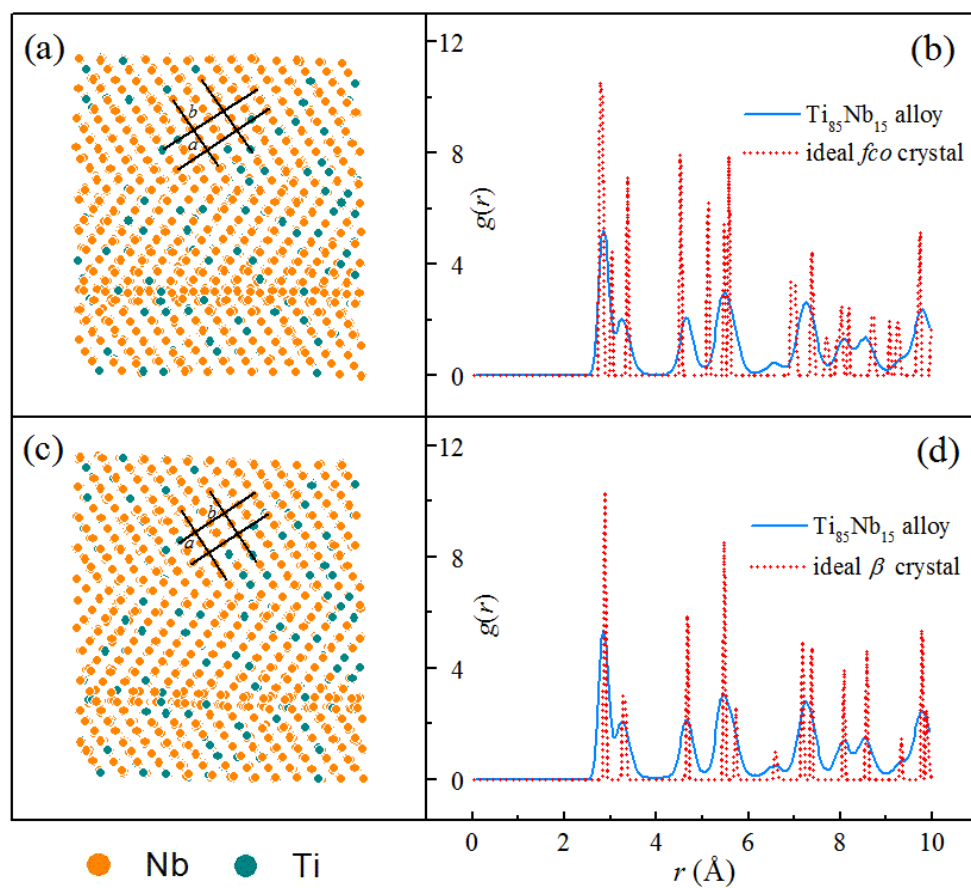


Figure 4. The distributions of atomic density $\rho(z)$ along z axis at 0.001 ns, 0.005 ns and 0.01 ns.

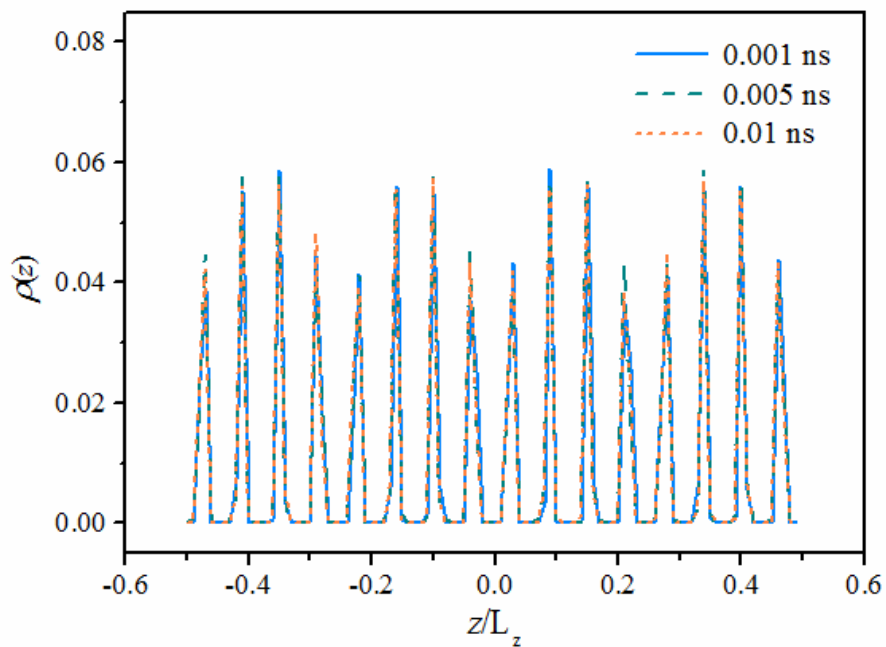


Figure 5. The atomic projections (x - y plane) of the second (orange dots) and third layers (dark cyan dots) of the simulated alloy at (a) 4000 time steps, (b) 5000 time steps, (c) 7000 time steps, and (d) 10000 time steps. Red dots denotes a hexagonal unit cell.

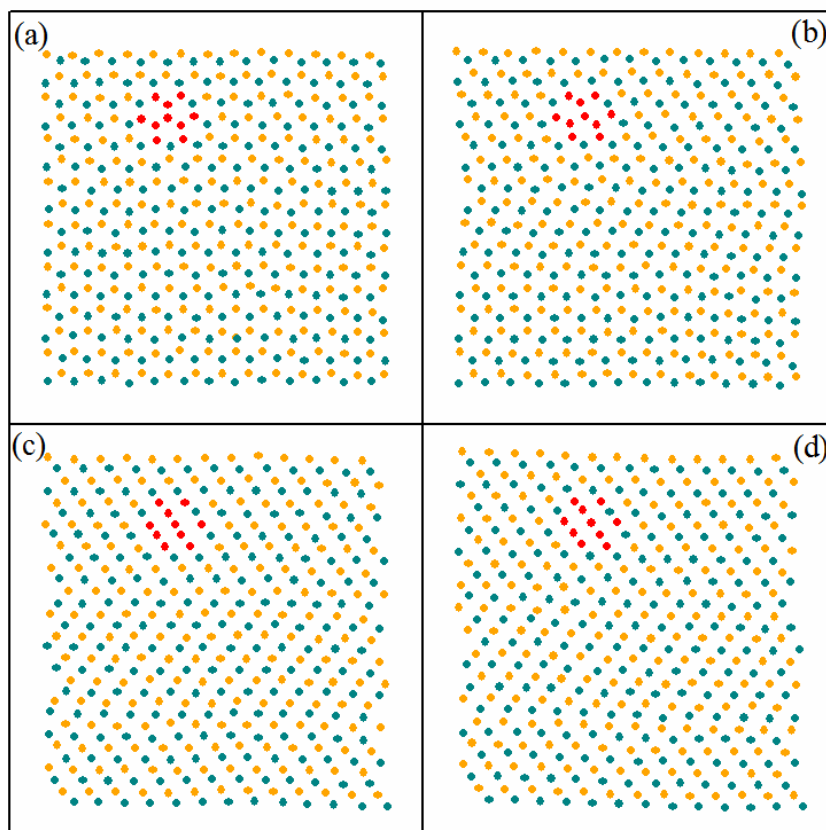


Figure 6. Variations of the enthalpy of the simulated atoms initiated from different structures as simulation time increased. The blue circles and curve represent the simulated atoms initiated from *hcp* structure; while the orange and green circles (curves) represent those initiated from *fco* and *bcc* structures, respectively.

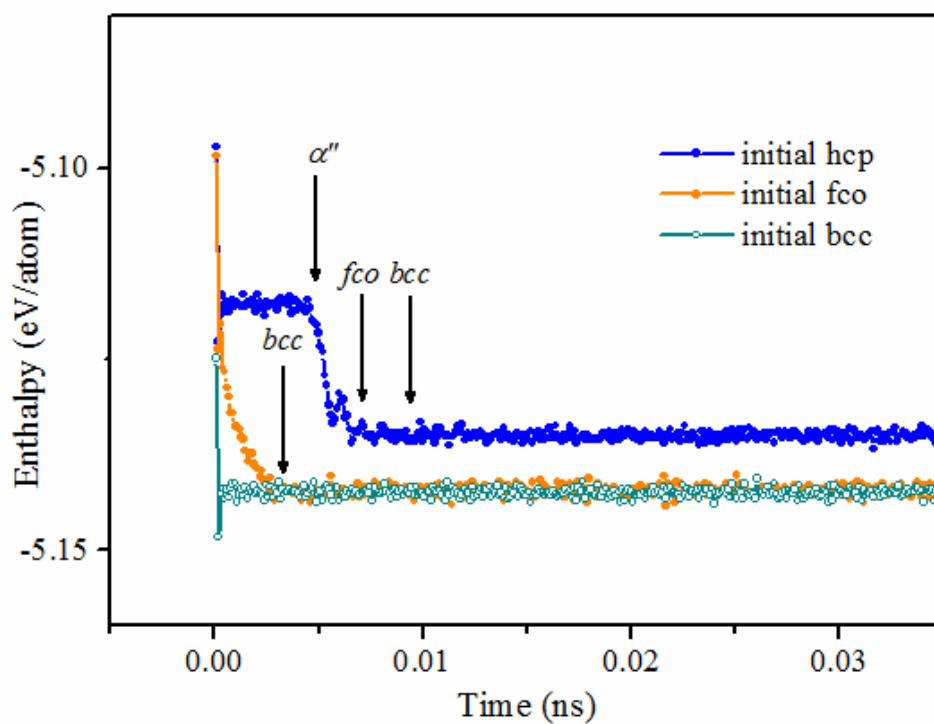


Figure 7. Schematic of geometric correlations among initial *hcp*, α'' and *fco* lattices on *x-y* plane. Open circles indicate the atomic positions of initial *hcp* lattice; green, and purple dots represent the atomic positions on $(0\ 0\ 0\ 2)_{hcp}$ crystal face after the slip; blue dots denote the atomic positions of the α'' lattice; orange big dots show the atomic positions of the *fco* structure.

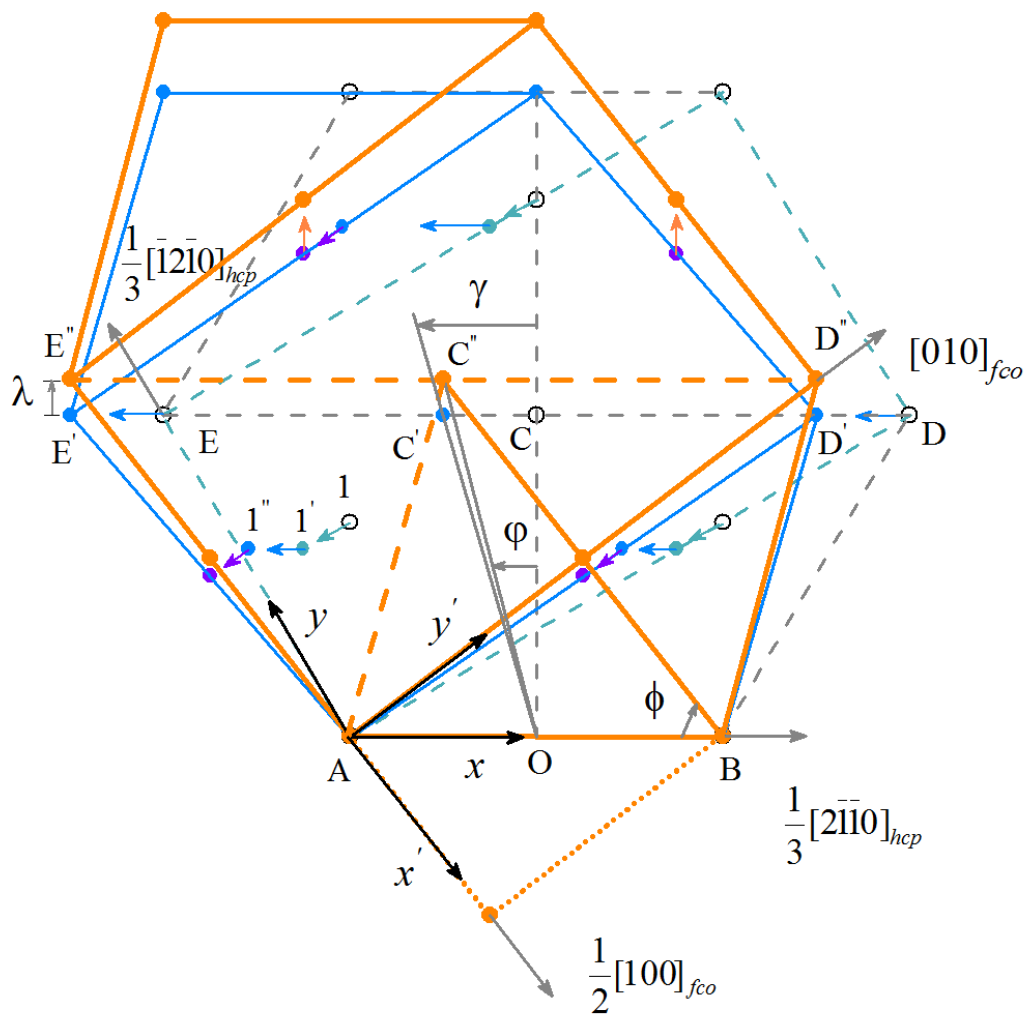


Figure 8. Schematic of geometric correlation of the *fco* and *bcc* lattices on *y-z* plane.

Blue solid lines denote the *fco* lattice, while red dash lines denote the *bcc* lattice.

